Experimental determination of thermodynamic properties of Hydrazine, MMH and NTO along the saturation line up to the critical point

Jouke Hijlkema, Marco de Rosa

DOI: 10.13009/EUCASS2019-297

DOI: ???

Experimental determination of thermodynamic properties of Hydrazine, MMH and NTO along the saturation line up to the critical point

Jouke Hijlkema* and Marco de Rosa†
ONERA* / ESA†
31410, Mauzac, France* / ESA †
jouke.hijlkema@onera.fr* / Marco.De.Rosa@esa.int†

Abstract

Thermodynamic properties as density and the speed of sound as a function of pressure and temperature are not very well-known for higher temperatures for typical storable propellants as Hydrazine, MMH or NTO. Most data is based on low temperature experiments that have been extrapolated or calculated from theoretical correlations. To our knowledge no experimental data exists up to the critical temperature except for a single experiment with Hydrazine that was carried out by Lobry de Bruyn [4] in 1896 and suffered from a catastrophic decomposition while trying to reproduce the results.

This paper deals with the design, development and use of an experimental installation capable of measuring the density and the speed of sound of the liquid phase as well as the density of the gaseous phase for these storable propellants from (close to) the triple point up to the critical point. Utmost care has been given to the safety aspects of the remotely operated installation. Low cost solutions have been devised to respect a rather tight budget. The installation is currently in its trial and calibration phase using pure water, this paper contains some results of these tests. The real propellant tests are bound to start in the coming months.

Glossary

moment of inertia	Quantity expressing a body's tendency to resist angular acceleration	$I(T)$	5
Density	Mass per unit volume	ρ	5
density measurement	Pixel correspoding to the position of the blade at temperature T	$Px(T)$	6
gravitational constant	Acceleration due to the atraction of the earth	g	5
speed of sound	propagation speed of sound in a medium	c	1, 8, 9
thermal expansion coefficient	Measure of the expansion of a material due to temperature changes	α	5
Young modulus	Measure of the stiffness of a material	$E(T)$	5
zero position for the density measurement	The pixel corresponding to the position of the unloaded blade	Z	6

1. Introduction

The determination of the density and the speed of sound for storable propellants like hydrazine or NTO is a complicated affair. Due to their inherent instability and toxicity, extreme care needs to be taken to avoid catastrophic events and protect personnel. This is the main reason why experimental data of this order is extremely rare.

ESA issued an invitation for tender in 2016 entitled "EXPERIMENTAL DETERMINATION OF STORABLE PROPELLANT PROPERTIES FOR MODELLING PURPOSES".

This article reflects the actual state of the research done at ONERA in this framework. A quick overview of the hardware components, their main functional principles and error estimations is followed by a section dealing with the calibration of the machinery. Some preliminary results from this calibration campaign will be presented as well.

DOI: 10.13009/EUCASS2019-297

2. Hardware

The hardware consists primarily of a high pressure vessel with 2 double-glazed sapphire windows. The external walls of the vessel are equipped with 1 kW electrical heaters. 2 isolation valves separate the test vessel from the rest of the hardware which comprises a buffer reservoir, a piston pump feed system, a neutralisation vessel, a vacuum pump, a purge system and a pressurisation system. The whole is operated by an in-house build, Raspberry Pi based, remote control and data acquisition system. The test vessel is supported by an iso-static positioning device that assures that the origin of vessel does not move due to thermal dilatation. This is important for the density measurements (see section 4.2 for details).

2.1 Pressure vessel

The pressure vessel is made of a titanium[1], cylindrical hollow body with matching titanium top and bottom covers. The outside is covered with 4 125 W lateral heater panels and each cover has a 250 W heater around its edge. Optical access is provided by 2 double surface sapphire windows that allow for a direct view of the internal cavity from 2 opposite sides (See figure 1b for an impression). Because of the nature of the test fluids, it is not possible to plunge a thermocouple directly inside the fluid. Therefore, 2mm diameter holes have been drilled in the vessel wall up to 1 mm from the surface of the internal cavity that allow for the placement of 4 thermocouples as close to the test fluids as possible. The vessel is designed with a burst pressure of 450 bars and has been successfully subjected to a hydrostatic proof pressure test up to 385 bars.

2.2 Remote control and data acquisition system

To reduce the risks for personnel to a maximum, the test set-up is remote controlled for all but one operation (the filling of the buffer reservoir with the test fluid). This is done through an in-house built remote control and data acquisition system depicted in figure 2. A supervisor (a Python program running on a laptop) is connected to our local network as well as a NAS, the main pilot and the pump pilot.

The last 2 are Raspberry Pi mini-computers situated next to the experimental set-up. Network communication is based on the excellent ZeroMQ library [2].

The main pilot talks to a DAC[3] over a USB link and operates the valves, heater and lights by means of a in-house built controller card (see figure 1e). The pump pilot controls the stepper motor control card that drives the feed system.

A separate (also in-house built) video control system is running on a pc in the remote control room (my desk) at a safe distance from the experiment. This machine controls the live streams from cameras around the set-up as well as the density camera (see section 4.2)

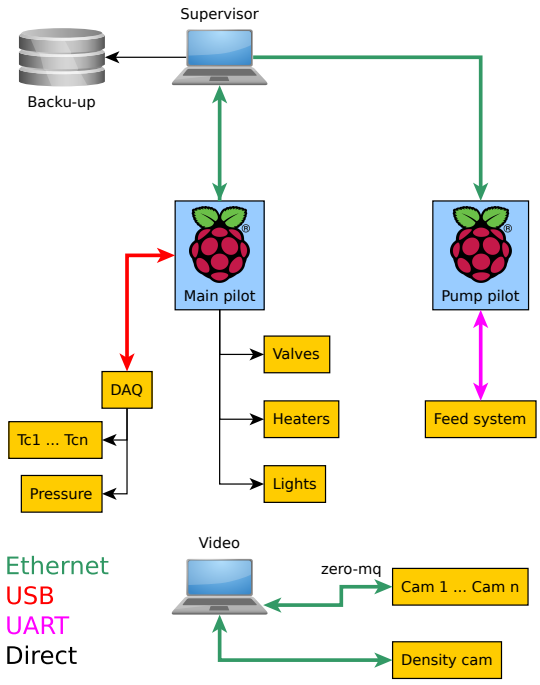

Figure 2: Remote control system

2.3 Feed system

The feed system consists of a stepper motor operated piston pump, a 3 way valve and a buffer reservoir. All wetted surfaces are in Teflon to ensure material compatibility. Table top experiments have shown a precision better than 0.01 ml. Figure 1d shows the entirety of the feed system. Before the experiment we fill the buffer reservoir with argon to chase all the air up to V1 (see figure 1a). Then, valves V5, V4, V3, V2 and V1 allow us to create

[1] Ta6V because of the material compatibility constraints
[2] http://zeromq.org/
[3] https://www.acquisys.fr/product/usb-1608g/

DOI: 10.13009/EUCASS2019-297

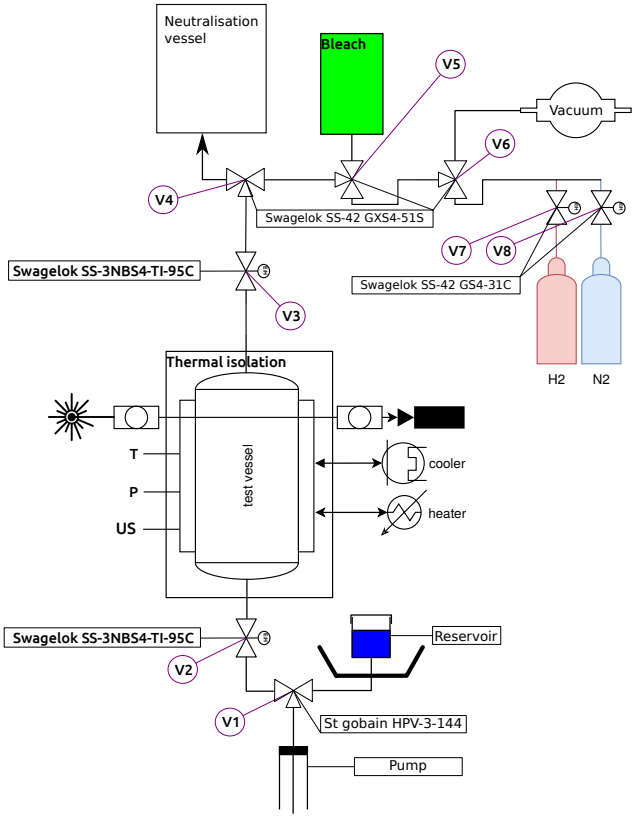

(a) Functional schematic

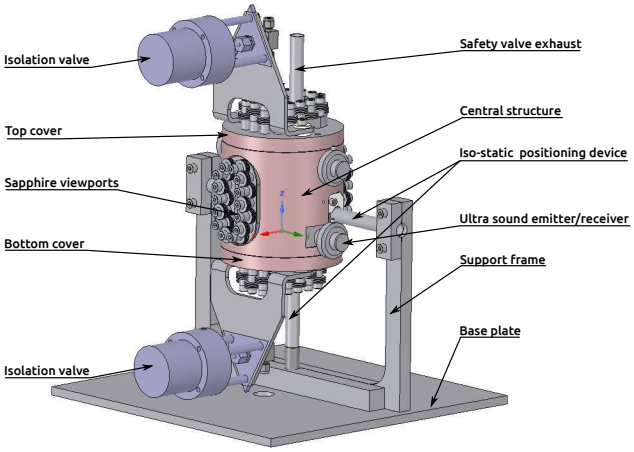

(b) Hardware components

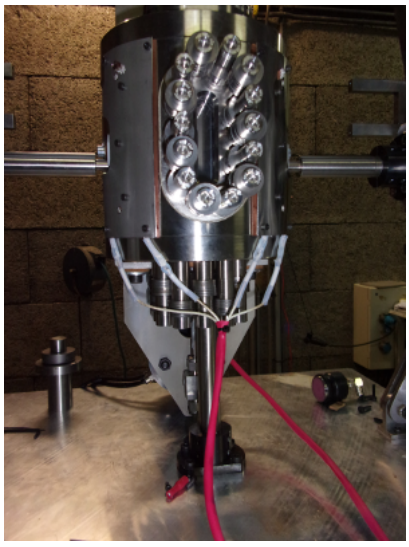

(c) Vessel & lateral heaters

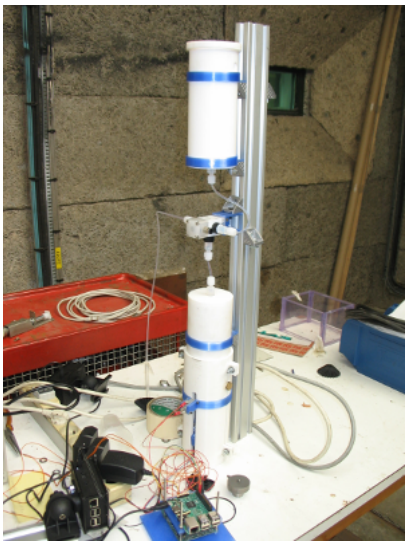

(d) Feed system

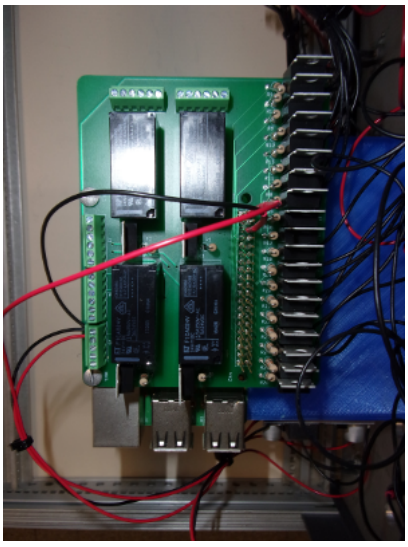

(e) Controller card

Figure 1: Hardware overview

a vacuum inside the vessel. Once the desired pressure drop has been achieved, we close V3 and toggle V4 so that in case of an emergency opening V3 will evacuate the product through the neutralisation vessel. We zero the density measurement system (see section 3), fill the buffer reservoir with the desired quantity of the test fluid (approximately 100 ml), close the lid and leave the test room. This is the only human intervention, the rest of the operations are piloted from a safe distance (200m).

DOI: 10.13009/EUCASS2019-297

2.4 Neutralisation vessel and purge system

Once the experiment is completed the vessel needs to be decontaminated and purged before any human intervention. The entrance of the neutralisation vessel has a diameter of 1 mm to make sure the flow is choked for high pressure conditions to limit the mass flow. The vessel is filled by 2/3 with silicon grit. Before the experiment we top off the grit with a neutralisation fluid (water for NTO or bleach for hydrazine and MMH). With the vessel at a sufficiently high temperature we open the upper isolation valve V3 and route the exit through the neutralisation vessel by using valve V4 (see 1a). The rest heat in the 15 kg heavy test vessel is sufficient to evaporate all the liquid in the system and the high pressure will chase the major part of the product through the neutralisation fluid. The silicon grit breaks the bubbles and extends the transit time and hence the exchange with the neutralisation fluid. The exit of the neutralisation vessel is connected to a closed container that collects the resulting run-off liquid.

Once the system has cooled down sufficiently we operate valves V5, V4, V3, V2 and V1 as well as the feed system pump to rinse all of the interior. The reservoir has an overflow port that connects to the same run-off container. Cameras at both the (transparent) exit of the neutralisation vessel and the reservoir overflow port allow us to verify that both extremities of the system have been rinsed.

3. Measurement systems

3.1 Data acquisition, pressure and temperature measurements

3.2 DAQ

Data acquisition is ensured by an in-house built machine since our existing acquisition system is not suited for experiments that take up to 8 hours. We use a Acquisys USB-1608G[4] DAQ. These machines have 16, 16 bit, analogue input ports and are capable of a total acquisition frequency of 250 kHz (multiplexed). Data is extracted over a USB link using the Python uldac package[5] and send to the supervisor for storage every 10 seconds. The supervisor sends a copy to the NAS for safe keeping. To reduce noise, temperature and pressure measurements are repeated 1000 times and averaged for each measurement point. This results in a total maximum data acquisition frequency of around 1 Hz.

3.2.1 Thermocouples

Since all known temperature sensors are incompatible with one or more of the storable propellants, the thermocouples (classical type K with a maximum continuous temperature of around 1100 °C) that will monitor the temperature in the test cavity are placed inside the wall of the test cell in holes drilled to within 1 mm of the inner cavity. These thermocouples need to be calibrated *in situ* in order to take into account the heating of the section of the wiring that touches (or is close to) the hot surface of the test vessel since the correspondence of the measured potential and the actual temperature difference between the thermocouple and the cold junction of type K thermocouples are given for a homogeneous cable temperature. A secondary objective of these calibration test runs is the determination of the time needed for the system to reach thermal equilibrium. When in equilibrium, the temperatures measured inside the wall are considered to be equal to the temperature of the test fluids. To verify this hypothesis a port in the upper cover of the vessel allows the passage of 2 thermocouples. These are plunged in the liquid and the gaseous phase. Once the calibration phase was over this port has been welded shut to prevent micro leakage as much as possible. Section 4.1 deals with these calibration runs.

3.2.2 Pressure transducers

Pressure is measured using GE UNIK 5000 pressure transducers [6]. For the measurements from ambient to critical pressure a 500 bar max range is used. For the measurements from ambient to the triple point pressure we use a 1 bar max range. These sensors have a combined accuracy of ± 0.04% full scale. This gives a precision of 200 mbar for the 500 bar max range and 0.4 mbar for 1 bar max range.

[4] https://www.acquisys.fr/product/usb-1608g/
[5] https://github.com/mccdaq
[6] https://www.gemeasurement.com/sites/gemc.dev/files/unik_5000_datasheet_english.pdf

DOI: 10.13009/EUCASS2019-297

3.3 Liquid phase density measurements

3.3.1 Principle

The principle of the density measurements is simple. As shown in figure 3, a floater of volume $V = d^3$ exerts a force F on the tip of a titanium blade.

If we ignore the influence of the pressure on the elasticity of the titanium blade then the deformation δ is a function of the temperature T and the density of the fluid $\rho(T)$:

$$\delta(T) = \frac{F(T)L^2(T)}{3E(T)I(T)}\,(L(T) + 0.5l(T)) \tag{1}$$

with $E(T)$ the Young modulus of TA6V as a function of temperature and $I(T)$ the moment of inertia. If we define $\beta_T = 1 + \alpha(T - T_0)$ with $\alpha = 9.10^{-6}\ m/m°C$, the thermal expansion coefficient of TA6V, we can express any dimension $D(T)$ as $D(T) = D_0\beta_T$. Then equation (1) becomes:

$$F(T) = \frac{\delta(T)E(T)WH^3\beta_T}{4L^2(L + 0.5l)} = \delta(T)E(T)\beta_T\Gamma \tag{2}$$

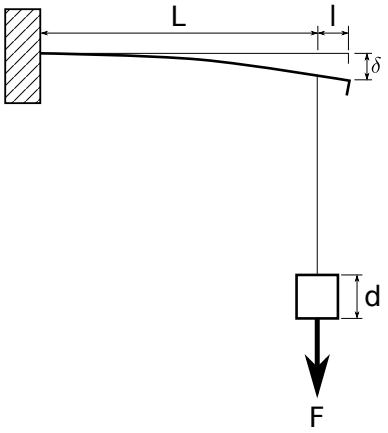

Figure 3: Principle

where W and H are the width and height of the blade and $\Gamma = \frac{WH^3}{4L^2(L+0.5l)}$. We know that $F(T) = g(m_f - \rho(T)d^3\beta_T^3)$ with m_f the mass of the floater so we can rewrite equation (2) as:

$$\rho(T) = \frac{m_f g - \delta(T)E(T)\beta_T\Gamma}{gd^3\beta_T^3} \tag{3}$$

Classically the temperature dependency of the Young modulus of a metal is considered linear and can be written as

$$E(T) = E_0(1 - a\frac{T}{T_m}) = a + bT$$

Table 1 shows the dependency of the Young modulus on temperature as determined by Julien et al.[2] which allows to coherently determine $a = 109.954$ and $b = -0.0698$

E (GPa)	T (°C)
108	28
30	1031

Table 1: Young's modulus as a function of temperature

Using the dimensions in table 2 we find that:

$$\rho(T) = \frac{0.042585 - 1.11932.01^{-10}\delta(T)E(T)\beta_T}{9.81^{-6}\beta_T^3} \tag{4}$$

W	0.01 m
H	0.0002 m
d	0.01 m
L	0.0556 m
l	0.0044 m
m_f	0.004341 kg

Table 2: dimensions of the system

This allows to determine the density of the test liquid knowing the temperature T and the deformation $\delta(T)$.

DOI: 10.13009/EUCASS2019-297

The experimental set-up measures $\delta(T)$ indirectly as the position of a mark on the blade in an image captured with an IDS UI-5480S[7] camera equipped with a SIGMA APO Macro 180 mm 1:3.5 D lens. The correspondence between the recorded pixel and the deformation $\delta(T)$ is related to the size of the pixels and the magnifying factor of the optics on one hand and the zero (vertical position of the camera) corresponding to the unloaded blade. This can be expressed as a linear transformation

$$\delta(T) = c * (Px(T) - Z) \tag{5}$$

where $Px(T)$ is the pixel recorded for a temperature T and Z is the pixel corresponding to the position of the unloaded blade. The coefficient c is related to the pixel size and the optics and can be supposed constant between experiments, Z, however, is sensible to eventual disturbances (movement of the camera or the vessel during preparations, thermal expansion during the test runs is countered by the iso-kinetic support of the test vessel) and needs to be determined before each test. To determine c we fit equation (5) to the results of a calibration run with water. Figure 8 shows the results of this operation giving $c \approx 7.366.10^{-6}$. Now the only thing left is to determine Z before each test. This is easy, we simply record the pixel Px_0 corresponding to position of the blade after pulling a vacuum and before filling the vessel. We know that this corresponds to the deformation due to the weight of the floater (see table 2) and with equation (4) and the hypothesis that $E(T) = E = 108$ GPa and $\beta_T = 1$ we see that the corresponding displacement δ_0 is equal to:

$$\delta_0 = \frac{0.042585}{1.11932.01^{-10}108.10^9} \approx 0.003523 \text{ m} \tag{6}$$

then

$$Z = Px_0 - \frac{\delta_0}{c}$$

3.3.2 Error estimation

The error estimation for the density measurements can be divided in two.

- The errors due to non-nominal behaviour (drops on the blade, bubbles on the floater, ...)
- measurement errors

The measurement errors are relatively easy to assess. We use the temperature measurements for which we have an error estimation $\epsilon_T \approx 1°$ (see section 4.1) and images from the camera that introduce an error $\epsilon_{Px} \approx 6$ pixels (from experience). For the other values the error does not come into play since they are constant and included in the calibration so the effective error is 0. Then, if we write the density as a function (see equation 4) of two independent variables $\rho(T, Px)$:

$$\rho(T, Px) = C_1 f(T) + C_2 g(Px) h(T)$$

with

$$\begin{aligned} C_1 &\approx 4.250.10^4 \\ C_2 &\approx 1.141.10^{-5} \\ f(T) &= \frac{1}{(1+\alpha T)^3} \\ g(Px) &= c(Px + Z) \\ h(T) &= \frac{a + bT}{(1+\alpha T)^2} \end{aligned}$$

Then we can express the error in $\rho(T, Px)$ as

$$\Delta\rho(T, Px) = \sqrt{\left(\Delta T \frac{\delta\rho}{\delta T}\right)^2 + \left(\Delta Px \frac{\delta\rho}{\delta Px}\right)^2}$$

so with

$$\begin{aligned} \frac{\delta\rho}{\delta T} &= C_1 f'(T) + C_2 g(Px) h'(T) \\ \frac{\delta\rho}{\delta Px} &= C_2 g'(Px) h(T) \end{aligned}$$

[7] https://en.ids-imaging.com/store/ui-5480se.html

DOI: 10.13009/EUCASS2019-297

and

$$\begin{aligned} f'(T) &= -\frac{\alpha}{3(1+\alpha T)^4} \\ g'(Px) &= c \\ h'(T) &= \frac{b}{1+\alpha T} - \frac{\alpha(a+bT)}{2(1+\alpha T)^3} \end{aligned}$$

we find

$$\Delta\rho(T, Px) = \sqrt{\Delta T^2 \eta(T, Px) + \Delta Px^2 \zeta(T, Px)}$$

with

$$\begin{aligned} \eta &= \left(-C_1 \frac{\alpha}{3(1+\alpha T)^4} + C_2 g(Px)\left(\frac{b}{1+\alpha T} - \frac{\alpha(a+bT)}{2(1+\alpha T)^3}\right)\right)^2 \\ \zeta &= \left(C_2 c \frac{a+bT}{(1+\alpha T)^2}\right)^2 \end{aligned}$$

The displacement of the blade is less than 1 mm so $g(Px)$ is inferior to 10^-3. This permits us to fill the following table

T	η	ζ	$\Delta\rho$ (kg/m^3)
0	0.016256250	8.5399786e-17	0.1275
100	0.016168742	7.4364279e-17	0.12715637
200	0.016081783	6.4161525e-17	0.12681397
300	0.015995369	5.4775107e-17	0.12647280
400	0.015909497	4.6188863e-17	0.12613285

Table 3: error estimations

The error due to non nominal behaviour is a lot harder to assess. However, the calibration tests can give us an idea. If we look at figure 8 and we assume that for the third measurement point the error is due to this type of behaviour we see that we would find $\rho \approx 780$ kg/m^3 instead. An error of 15 kg/m^3, 100 times bigger than the typical error in table 3 but still lest than 2%.

3.4 Gas phase density measurements

3.4.1 Principle

Once the liquid phase densities are obtained, the gas phase density can be derived as follows. An insert made out of titanium divides the vessel in a lower and upper volume separated by a narrow channel passing in front of the windows. This channel allows for the precise determination of the liquid volume.

Figure 4 shows a schematic overview. Given the liquid density ρ_l measured previously (see section 4.2) and the total mass m_t of the product, the volume change observed in the capillary section of the cell is a measure of the gas density.

$$\begin{aligned} V_g &= V_t - V_l \\ \rho_g &= \frac{m_t - V_l \rho_l(T, P)}{V_g} \end{aligned}$$

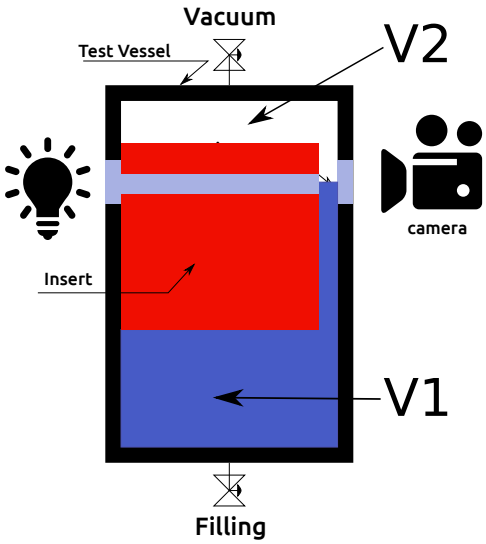

Figure 4: Principle

3.4.2 Error estimation

If we state that $m_t = V_l \rho_l$ then we see that the gas density depends on the measurement of the liquid volume, the injected mass as

DOI: 10.13009/EUCASS2019-297

$$\rho_g(m_t, vl) = \frac{m_t - V_l \rho_l}{V_g}$$

and we can estimate the measurement error as

$$\Delta\rho_g = \sqrt{\left(\Delta m_t \frac{1}{V_g}\right)^2 + \left(\Delta V \frac{m_t}{V_g^2}\right)^2}$$

So, with $V_g \approx 2500\ mm^3$, $\Delta V \approx 5\ mm^3$ we get the error estimation given in table 4. It should be noted that this does not take into account the error in the liquid density (see section 3.5.2)

Product	ρ_l	Error
NTO	550	7.2728373^{-4}
	1500	2.6669666^{-4}
MMH	290	1.3793161^{-3}
	950	4.2107163^{-4}
Hyd	230	1.7391350^{-3}
	1030	3.8837011^{-4}

Table 4: gas density error estimation

3.5 Liquid speed-of-sound measurements

3.5.1 Principle

The speed of sound is measured in the liquid phase by means of an emitter/receiver pair of ultrasonic sensors[8]. These sensors are not able to withstand high temperatures and are therefore retractable. We measure the time of flight of the ultrasonic wave through the test vessel and the test liquid (see figure 5). Then we know that

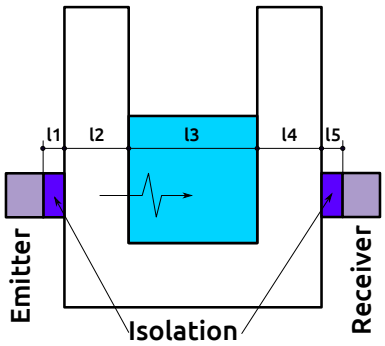

Figure 5: Principle

$$t_{flight} = t_{ext} + t_{cav} = \frac{l_{ext}}{c_{ext}} + \frac{l_{cav}}{c_{liq}}$$

where $l_{ext} = l_1 + l_2 + l_4 + l_5$ and t_{ext} is the flight time of the pulse through l_{ext}. The second term $\frac{l_{cav}}{c_{liq}}$ is the flight time through the cavity. If we ignore the influence of the internal pressure on the path lengths (at 345 bars, the maximum deformation of the vessel is 0.082 mm for an initial dimension of the order of 50 mm hence in the order of 0.15%) than the path lengths l_{ext} and l_{cav} are dependent only on the temperature through the thermal expansion coefficient α

$$l_{ext}(T) = l_{ext}(T_0)(1 + \alpha(T - T_0))$$
$$l_{cav}(T) = l_{cav}(T_0)(1 + \alpha(T - T_0))$$

The value for α can easily be found in the literature [[5], [6]].

Now if we do a calibration run with water as the test fluid in which we measure the flight time $t^{H_2O}(T, P)$ as a function of the temperature and pressure we can write

$$t_{ext}(T) = t^{H_2O}(T, P) - \frac{l_{cav}(T)}{c^{H_2O}(T, P)}$$

where $c^{H_2O}(T, P)$ can be found in the literature [[3][1]] and all the other terms are known. Once we have $t_{ext}(T)$ (which is independent of the test fluid and the pressure) we can use it to determine $c^{prod}(T, P)$ for all of our test fluids by measuring the flight time $t^{prod}(T, P)$

[8] http://www.epsilon-ndt.com/upload/file/problar-ve-aksesuarlar-.pdf

DOI: 10.13009/EUCASS2019-297

$$c^{prod}(T,P) = \frac{l_{cav}(T)}{t^{prod}(T,P) - t_{ext}(T)} \tag{7}$$

During the calibration tests we will determine t_{ext}, this is not finished yet.

3.5.2 Error estimation

Equation (7) allows us to write:

$$\Delta c(t^{prod}) = \Delta t^{prod} \frac{C1}{(t^{prod} + C2)^2} \tag{8}$$

With $C1 \approx 0.07$ and the values found in table 5 we expect that $t^{prod} - C2 \in [3.3.10^{-5}, 9.3.10^{-5}]$.

Product	c_{min}	c_{max}
NTO	840	1100
MMH	1200	1700
Hydrazine	1800	2100

Table 5: speed of sound expectations

If we assume that the error in the measurement of the flight time is of the order of the ultra sound frequency, that is 10^{-6} (we wont make an error of more than one cycle) then

$$\Delta c(t^{prod}) \in [8.1, 64.3]\ m/s$$

this is an error of between 0.96% and 3.1 %.

3.6 Gas phase speed-of-sound measurements

Due to the large difference in density between the titanium body of the vessel and the gaseous part of the propellant it is not possible to use the same ultra sound technique as used for the liquid phase (see section 3.5). A completely different approach has been tested to deal with this.

The gas trapped above the liquid phase forms a cavity that we can try to excite acoustically by making the walls vibrate with a well chosen frequency sweep. If we then measure the unsteady component of the gas pressure we should be able to determine the resonance frequency F_{res} and hence the speed of sound inside the gas (We assume the longitudinal dimension L of the cavity known, this is valid since the eventual dilatation effects due to the temperature variation and pressure will be detected during the calibration runs and can be taken into account)

$$C = F_{res} * 2 * L(T,P)$$

3.6.1 Proof of concept

As a proof of concept the following test setup has been devised (cf. figure 6):

- An aluminium, closed box equipped with a Kistler pressure transducer hooked up to a Kistler charge amplifier (CA).
- A piezo vibrator glued to the side of the box and hooked up to a signal generator.

Both the charge amplifier and the signal generator are connected to and controlled by the main pilot (see section 2.2) through a USB port (this allows us to adjust the range and sensitivity of the system as well as the signal characteristics if need be during operations). The Charge amplifiers output is read by the DAQ and transferred to the main pilot. This set-up does not allow for a precise synchronisation of the recording with the signal generator. This is not a problem if we use a double sweep.

The signal generator is programmed to do a double sweep going from 1000 Hz to 5000 Hz and back to 1000 Hz in 20 seconds (10 up, 10 down). The temperature of the air is 25°C so we should measure a speed of sound of 2662 Hz.

Figure 6c show the results of the test. We note the nice symmetries of the resonance peaks and the fact that the recording is not synchronised (the signal is not symmetrical, we miss the tail of the sweep because the recording starts before the sweep. The double sweep avoids the need for a perfect synchronisation of the sub systems).

DOI: 10.13009/EUCASS2019-297

The analysing software finds the biggest 2 peaks and determines the center of the sweep (the middle between these peaks). This is the gray line in the figure. Then we find the lesser peaks and since we now know the time difference D between the center and the peaks, the start frequency F_s and the center frequency F_c of the sweep and the half sweep duration S_d we can calculate the peak frequencies as:

$$F1 = F_c - \frac{D(F_c - F_s)}{S_d}$$
$$F2 = F_c + \frac{D(F_c - F_s)}{S_d}$$

We look for peaks with decreasing amplitudes until we find one that is close to our initial guess of the speed of sound (given the graph this does not have to be very precise)

The red lines in the graph represent the values found and we note that the algorithm detects the extremes very nicely. The blue lines in the graph that correspond to the theoretical value of 2662 Hz are invisible since they are nearly fully covered by the red lines (2676.8 Hz). We're off by less than 0.6%! If need be we can adapt the sweep characteristics to be closer to the resonance frequency, this should further increase the acuracy.

3.6.2 Actual experimental set-up

In the actual set-up the walls are much to thick to directly transfer the movement of the vibrator and to induce a P' at the surface of the cavity. Since the prime interest of the vessel walls is to withstand the pressure inside the cavity, a very limited number of options are feasible. We've opted for a tunnel drilled into the wall that stops 5 mm from the inner surface. A free floating cylinder acts as a plunger to transmit the movement of the vibrator to the surface of the vessel. (see 6d to get the idea). Sadly this does not work, we tried different vibrators but there is no resonance signal measurable. The most plausible explanation is that the surface of the inner wall that transmit the vibrations is just not big enough to provoke a resonance phenomena. We will therefore refrain from the measurement of the speed of sound in the gas phase. The Kistler pressure transducer was supposed to be mounted on the top port that allowed for the thermocouples used during the calibration runs (see section 3.2.1).

4. Calibration

4.1 Pressure transducers and thermocouples

The pressure sensors are calibrated using a calibration balance present at ONERA. Before every test run the sensor is zeroed against the atmospheric pressure (given to be precise within a range of ± 10 Pa).

During these calibration tests 2 thermocouples are placed inside the cavity (on in the liquid and one in the gaseous phase, see section 3.2.1). These thermocouples permit to quantify the temperature difference between the embedded thermocouples and the actual temperature in the cavity as well as the eventual temperature in-homogeneity between the liquid and the gaseous phase.

The reference temperature is obtained through the pressure measurements. For pure water, injected under vacuum conditions, the relation between pressure and temperature is known perfectly well. A typical test run is given in figure 7a. At regular intervals (150°C,200°C,250°C ...) the system is left to go to equilibrium and a calibration point is obtained.

TC Id	a	b
Bottom rear	-0.0021	0.9880
Top rear	0.034	0.9817
Bottom front	0.0028	1.0087
Top front	-0.0013	0.9929

Table 6: TC transfer function coefficients

Figure 7b shows the perfectly linear behaviour of the thermocouples and table 6 gives the corresponding coefficients of the best fit for this calibration run. Figures 7c and 7d show the results of a verification run using the calibration coefficients found earlier. We see from figure 7c that the measured temperatures join the target temperature of 250 °C around 13:26. Figure 7d show that this corresponds to time when the pressure derivative becomes zero. The same figure show that the derivatives of the temperature measurements inside the cavity join the pressure derivative at 0 around

DOI: 10.13009/EUCASS2019-297

(a) Charge Amplifier and DAQ

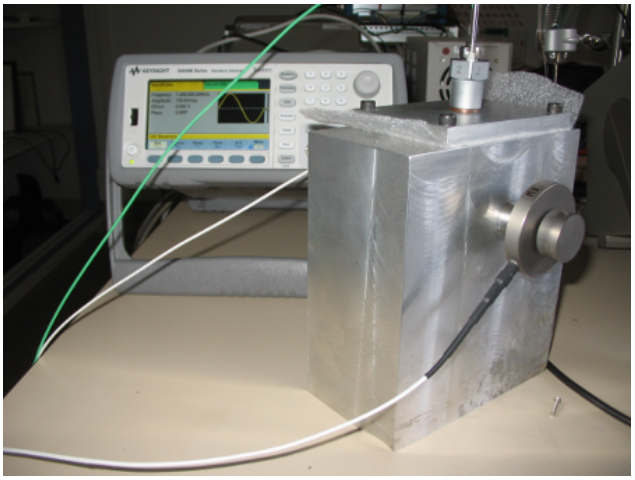

(b) Signal generator and test box

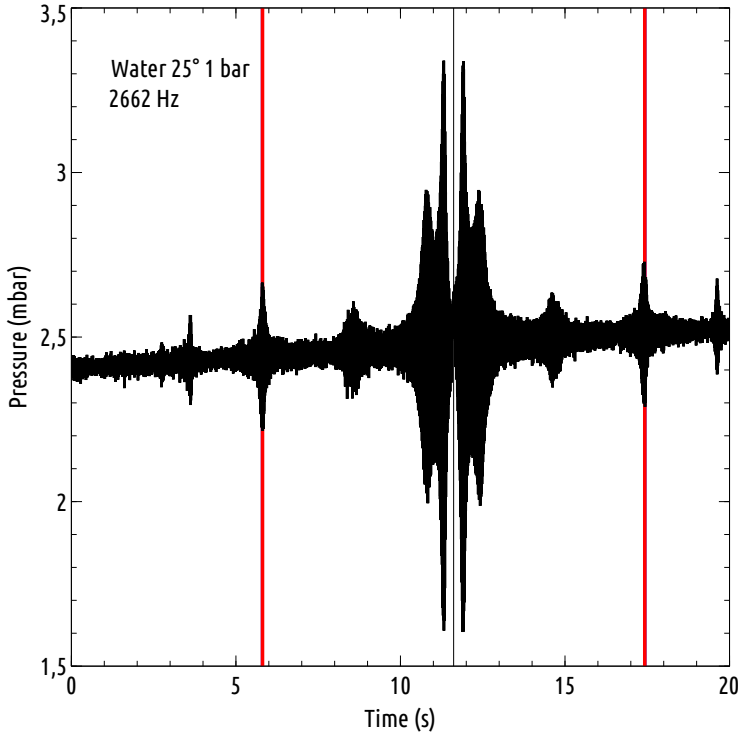

(c) Test results

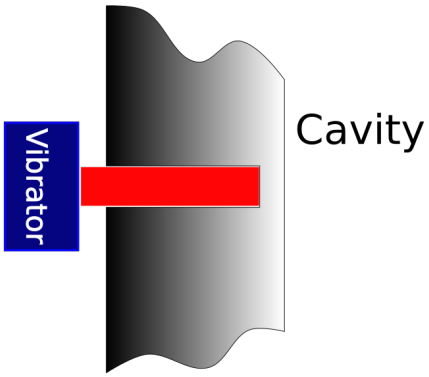

(d) Actual system

Figure 6: test setup

13:33, that is 6 minutes later. From figure 7c we extract the different temperatures (only the rear thermocouples were present during the test since the front thermocouples needed to be rerouted to make place for a camera). The values are given in table 7 and show a maximum difference of 0.77 °C.

4.2 Liquid phase density measurements

Once the temperature calibrations done, the port that was used to place two thermocouples inside the cavity was welded shut. The floater and balance system (see 4.2 for details) were installed and several test runs with pure water have been carried out. Table 8 shows the results as well the theoretical density $\rho_{th}(P,T)$.

So if we use T, P, Px and ρ_{th} and equation 6 and fit the data using equation 5 ($c = 7.366.10^{-6}$ and $Z = -468.14$) we find the results in figure 8.

DOI: 10.13009/EUCASS2019-297

TC id	Measured T (°C)
Bottom rear	246.40
Top rear	246.29
Gas	246.60
Water	247.03

Table 7: temperature readings at 13:33

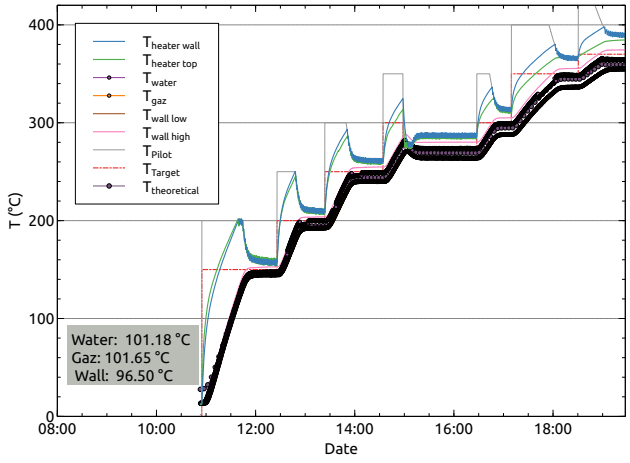

(a) Typical calibration run

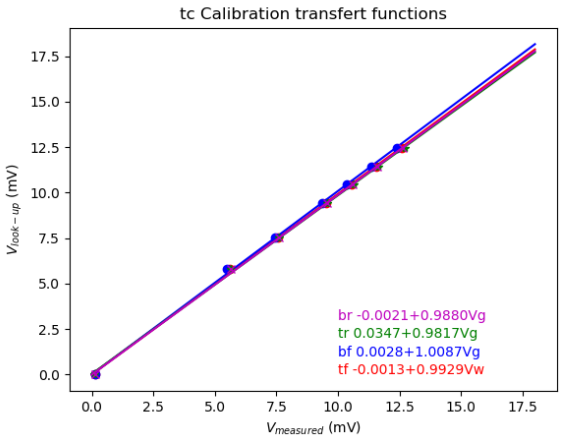

(b) Data fitting

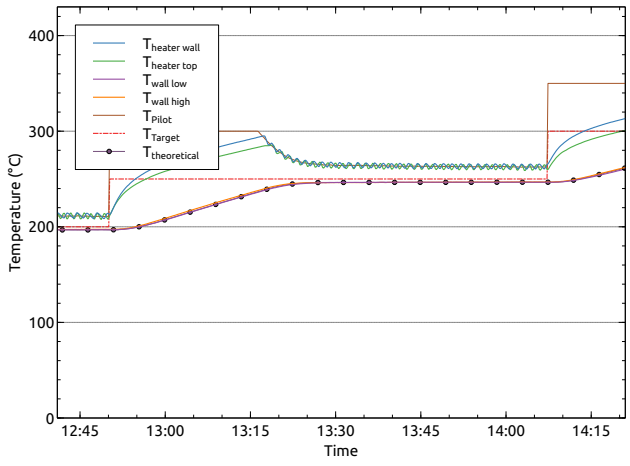

(c) Temperature

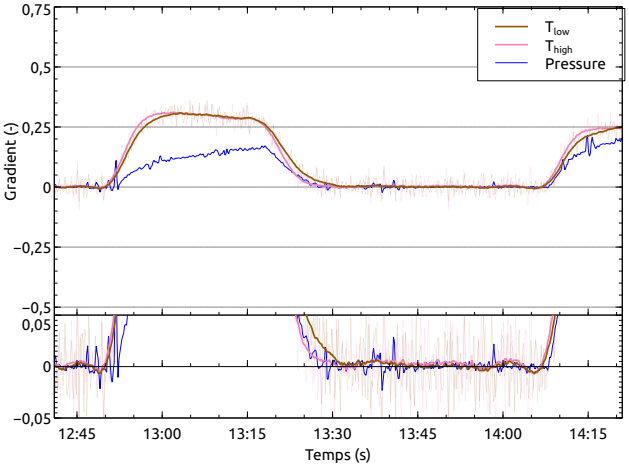

(d) Derivatives

Figure 7: Temperature verification run

The accuracy is really nice for such a rudimentary system. Especially considering that only one point of the curve is fitted.

DOI: 10.13009/EUCASS2019-297

$T\ (°C)$	$P\ (bar)$	$Px\ (-)$	$\rho_{th}\ (kg/m^3)$
318.0	110.5	968	672.0
294.0	79.4	950	724.2
269.6	55.4	926	768.1
245.13	37.2	916	806.0
196.11	15.126	896	869.2
147.33	5.346	876	919.5
13.77	0.972	836	999.2

Table 8: Density measurement calibration

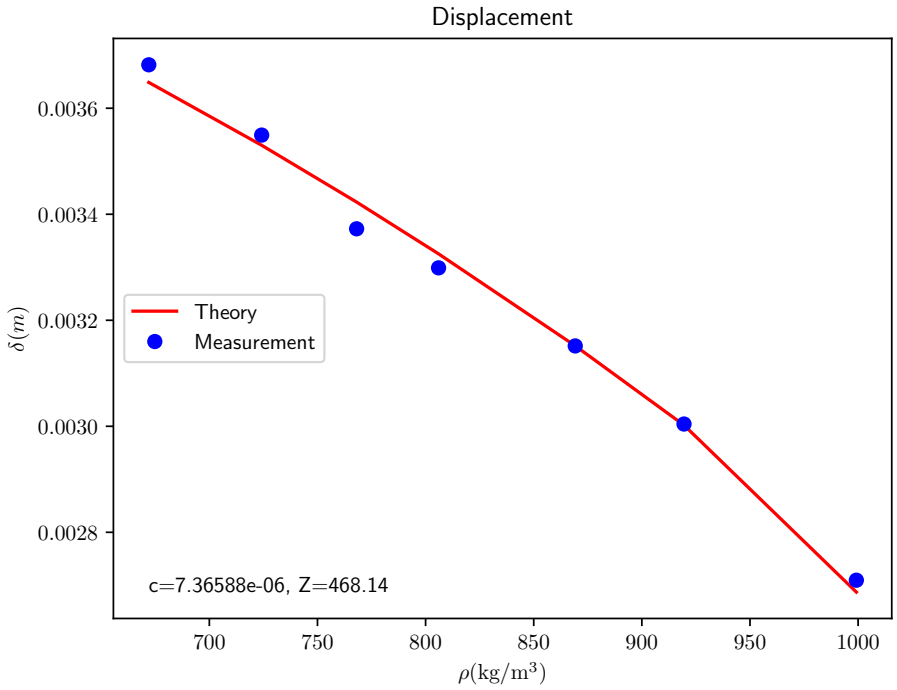

Figure 8: Calibration density measurements

5. Conclusion

The work presented in this paper is not finished. During the two years of activities a lot of things went wrong or not as expected and Murphy invited himself to the party a lot more than we had hoped. This is why we are not as far as we had initially estimated and this paper does not contain actual results of the real test fluids as we had hoped to be able to deliver at least partially.

The lessons learned are numerous and we continue to find ways to improve or circumvent the obstacles we constantly find on out way. At the moment I am writing this, the installation is again in hold since we blew a window at a pressure far below the test pressure of 385 bars. We are currently looking for an explanation and are replacing the broken parts.

There is only one more calibration run needed to calibrate the ultra sound measurements before we can start to tackle the real products, beginning with NTO.

Once the real propellant test are completed, we are looking forward to writing the sequel to this adventure. It is more and more clear to us why this has not been done since 1896 but we remain optimistic (most of the time) and persevere.

DOI: 10.13009/EUCASS2019-297

References

[1] Harold C Helgeson and David H Kirkham. “Theoretical prediction of the thermodynamic behavior of aqueous electrolytes at high pressures and temperatures; II, Debye-Huckel parameters for activity coefficients and relative partial molal properties”. In: *American Journal of Science* 274.10 (1974), pp. 1199–1261.

[2] Renaud Julien et al. “Characterization and modeling of forged Ti-6Al-4V Titanium alloy with microstructural considerations during quenching process”. In: *International Journal of Mechanical Sciences* 142 (2018), pp. 456–467.

[3] Susan Werner Kieffer. “Sound speed in liquid-gas mixtures: Water-air and water-steam”. In: *Journal of Geophysical research* 82.20 (1977), pp. 2895–2904.

[4] C. A. Lobry de Bruyn. “Free Hydrazine I. Recl”. In: *Trav. Chim* 15 (1896), pp. 174–184.

[5] M Lyakhovitskii et al. “Experimental investigation of acoustic properties of titanium alloys in the temperature range of 20-1000Â° C.” In: *High Temperature* 51.1 (2013).

[6] C Peytour, F Barbier, and A Revcolevschi. “Characterization of ceramic/TA6V titanium alloy brazed joints”. In: *Journal of Materials Research* 5.1 (1990), pp. 127–135.